

# Spectral structure of laser light scattering revisited: bandwidths of nonresonant scattering lidars

Chiao-Yao She

It is well known that scattering lidars, i.e., Mie, aerosol-wind, Rayleigh, high-spectral-resolution, molecular-wind, rotational Raman, and vibrational Raman lidars, are workhorses for probing atmospheric properties, including the backscatter ratio, aerosol extinction coefficient, temperature, pressure, density, and winds. The spectral structure of molecular scattering (strength and bandwidth) and its constituent spectra associated with Rayleigh and vibrational Raman scattering are reviewed. Revisiting the correct name by distinguishing Cabannes scattering from Rayleigh scattering, and sharpening the definition of each scattering component in the Rayleigh scattering spectrum, the review allows a systematic, logical, and useful comparison in strength and bandwidth between each scattering component and in receiver bandwidths (for both nighttime and daytime operation) between the various scattering lidars for atmospheric sensing. © 2001 Optical Society of America

*OCIS codes:* 290.5870, 290.3770, 010.1300, 290.5840.

## 1. Introduction

Application of the procedure of laser light scattering has led to a number of powerful lidar instruments for remote sensing of the atmosphere. As is well known, atmospheric information can be retrieved from two factors in the lidar equation: backscattering and extinction. When the laser frequency is far from an absorption line of atmospheric constituents, the scattering process is nonresonant. The returned signal then consists of Rayleigh scattering and vibration Raman scattering from molecules as well as Mie scattering from aerosol and clouds. With appropriate spectral filters these scattering components can be separated. The detection of individual components gives rise to Rayleigh lidar, Raman lidar, and Mie lidar. Although not well known to the physics community in general and to the lidar community in particular, a spectral structure exists in Rayleigh scattered light: a Doppler-broadened central peak, called the Cabannes line, and sidebands that are due to (pure) rotational Raman scattering. Cabannes<sup>1</sup> predicted the intensity and polarization of the center

peak, and Cabannes and Rocard<sup>2</sup> gave the relative intensities of the unshifted central peak and the shifted pure rotational Raman sidebands. Proper disentanglement and detection of the signal from these scattering processes give rise to high-spectral-resolution lidar (HSRL) and rotational Raman lidar, respectively. In this context we refer to Rayleigh lidar as a device that receives signals from both Cabannes and (pure) rotational Raman scattering.

In practice it is often difficult to separate various scattering components. In addition to scattering from aerosol and clouds, a Mie lidar often detects molecular (Rayleigh and vibrational Raman) scattering as well, but in circumstances of interest the latter is often negligible by comparison. On the other hand, a Rayleigh lidar for temperature measurements usually contains Mie scattering from aerosol, thus limiting its effectiveness to altitudes above<sup>3</sup> ~30 km. The need to reject a Mie-scattering signal for atmospheric temperature profiling at lower altitudes brought rotational Raman lidar (RRL) and HSRL into being.

Doppler wind lidar measures motion-induced Doppler shift for determining the line-of-sight wind velocity. Since the Doppler shift is very small, 40 MHz (2 MHz) for a 10-m/s wind at 0.5  $\mu\text{m}$  (10  $\mu\text{m}$ ), only a narrow-band system can be used to detect the fractional shift in the Doppler-broadened Cabannes spectrum. Unfortunately, this process is often incorrectly referred to in the literature as detecting a Doppler shift of Rayleigh (or a Rayleigh-Brillouin)

---

C.-Y. She (joeshe@lamar.colostate.edu) is with the Department of Physics, Colorado State University, Fort Collins, Colorado 80523-1785.

Received 13 October 2000; revised manuscript received 3 May 2001.

0003-6935/01/274875-10\$15.00/0

© 2001 Optical Society of America

spectrum. As mentioned the Rayleigh-scattering spectrum consists of the Cabannes line and rotational Raman sidebands. At  $0.5 \mu\text{m}$  the widths of the Cabannes line and Rayleigh spectrum are, respectively,  $2.5 \text{ GHz}$  and  $200 \text{ cm}^{-1}$ . A  $40\text{-MHz}$  shift amounts to approximately  $7 \times 10^{-9}$  of the width of the Rayleigh-scattering spectrum; it is not detectable by current instrumentation. In a high-density gas or condensed matter, the Cabannes line splits into a triplet resulting from entropy (a narrower central peak) and pressure (Brillouin-shifted Stokes and anti-Stokes lines) fluctuations. This triplet is termed the Rayleigh–Brillouin spectrum, again incorrectly, because it was not possible in Lord Rayleigh's time to resolve the Cabannes line from rotational sidebands as pointed out by Young,<sup>4</sup> let alone the triplet within the Cabannes line. Obviously one should not use the term Rayleigh scattering for both the central peak that is due to entropy fluctuations ( $<1 \text{ GHz}$  wide) and the entire Rayleigh spectrum ( $>100 \text{ cm}^{-1}$  wide), which in liquids consists of the triplet of fluctuation scattering and hindered rotational Raman scattering (often referred to as Rayleigh-wing scattering<sup>5</sup> in the literature, again incorrectly).

When the laser frequency approaches an absorption line of an atmospheric constituent, the scattering cross section in the near-resonance condition is significantly enhanced. Resonance Raman lidar<sup>6</sup> takes advantage of this enhancement, providing an effective means for the detection of trace species in the atmosphere. When the laser frequency is close enough to induce absorption, fluorescence often follows; the resonance (Rayleigh and Raman) scattering process then becomes the process of laser-induced fluorescence.<sup>7</sup> Although the polarization properties of these two processes differ, both their scattering cross sections are orders of magnitude larger than those of their nonresonant counterparts. Differential absorption lidar depends on the comparison between extinction coefficients resulting from the difference in the absorption coefficient between on- and off-resonance frequencies of a selected minor species.<sup>8</sup> Since the on-resonance-induced fluorescence is often quenched in the atmosphere, the returned lidar signal is mainly due to off-resonance backscattering from the majority species, giving differential absorption lidar an earlier (perhaps more appropriate) name, differential absorption and scattering lidar. Owing to the overwhelming enhancement in cross section, resonance fluorescence lidar should be a powerful tool for detecting the concentration of minor species and indirectly for measuring atmospheric-state parameters. Unfortunately, quenching resulting from collisions with nitrogen and oxygen molecules has rendered this process useless in the lower atmosphere. The anticipated power of fluorescence lidar can be realized and has been indeed demonstrated in the mesopause region for atmospheric dynamics studies<sup>9</sup> as well as for species detection in seawater and/or plants.<sup>10</sup> However, these studies are beyond the scope of this paper.

The purpose of this paper is, on the one hand, to

revisit the spectral structure of the nonresonant light-scattering processes, thereby calling attention of the lidar community to the different bandwidths associated with individual features in the light-scattering spectrum and advocating use of the correct definition and the name of each molecular-scattering component. On the other hand, in this paper I explicitly state the bandwidth and strength of each scattering component employed by a specific lidar measurement, thereby sharpening its definition and comparing the relative merits as well as difficulties associated with each nonresonant-scattering lidar technique used for atmospheric parameter measurements. No information presented below is new. Most of it was, however, presented piecemeal in the literature with different emphases. As the lidar technology matures and lidar measurements increasingly depend on narrow-band systems, I believe that there is a need for a concise, physically based description of the bandwidth and of the preferred (or historically correct) naming for each component of the atmospheric light-scattering spectrum to advance the conceptual understanding and to sharpen the relationship and relative merits between various scattering lidars in different atmospheric conditions. It is hoped that this paper serves such a need.

## 2. Spectrum of Light Scattering by Major Species in the Atmosphere

It is well known that when excited off resonance, an atom in the ground state (spherically symmetric) at rest scatters light elastically. Its cross section can be calculated quantum mechanically. In honor of Lord Rayleigh, who discovered molecular scattering, we call it Rayleigh scattering.<sup>11</sup> The spectrum of scattered light for a collection of low-density atoms in equilibrium at temperature  $T$  is Doppler broadened. Inasmuch as atoms do not rotate or vibrate, there can be no sidebands in the scattering spectrum. Although debatable, calling such a single Doppler-broadened line the Rayleigh spectrum at least causes no confusion. However, a molecule in its electronic ground state rotates and vibrates. These motions lead to inelastic scattering and yield a characteristic scattering spectrum. For diatomic molecules, such as nitrogen and oxygen, the spectrum of the inelastically scattered light appears orderly but with complex sidebands. Late Nobel Laureate, Art Schawlow, in his many delightful lectures called a diatomic molecule “a molecule with one atom too many.”

A typical nonresonant light-scattering spectrum from a collection of monodisperse diatomic molecules at temperature  $T$  is schematically displayed in wave number in Fig. 1 by use of nitrogen molecules at  $275 \text{ K}$  as an example. The excitation (incident) wavelength is taken to be  $532 \text{ nm}$  (or  $18,797 \text{ cm}^{-1}$ ). To understand the structure of this spectrum, we first model the diatomic molecule as a rigid rotor. As such, there are two independent parts in the polarizability, isotropic part (or trace)  $\alpha$  and anisotropic part  $\gamma$  whose squares are, respectively, proportional

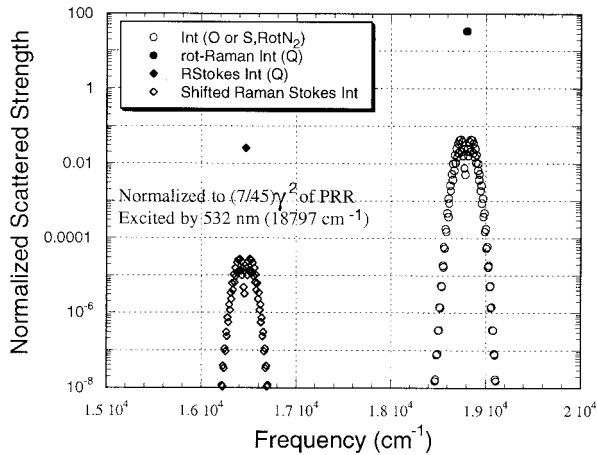


Fig. 1. Rayleigh and Raman spectra of  $N_2$  at 275 K. At this temperature the vibrational anti-Stokes intensity is negligible.

to cross sections of polarized (or coherent) and depolarized (or incoherent) scattering. Polarized scattering, such as that from atoms, is not affected by molecular rotation. Scattering by molecular anisotropy, affected by rotational motion of the molecule, can be separated into three branches in the frequency spectrum, the unshifted  $Q(\Delta J = 0)$  branch, and the shifted  $O(\Delta J = -2)$  and  $S(\Delta J = 2)$  branches, where  $J$  denotes the rotational quantum number of the molecule. The  $O$  and  $S$  branches consist, respectively, of blueshifted and redshifted sidebands that correspond to anti-Stokes and Stokes pure rotational Raman scattering. For clarity in this paper I stress that the central Cabannes line consists of the polarized scattering and the unshifted (or  $Q$  branch of) depolarized scattering, whereas rotational Raman scattering refers to the  $O$ - and  $S$ -branch sidebands of the depolarized scattering only.

The relative strengths (probabilities) between the three branches of the depolarized scattering, depending on the rotational quantum number of the initial state  $J$ , are given by Placzek and Teller factors<sup>12</sup> or probabilities<sup>13</sup> such as

$$\begin{aligned}
 P_O(J \rightarrow J - 2) &= 3J(J - 1)/2(2J - 1)(2J \\
 &\quad + 1) \rightarrow 3/8 \quad \text{for the } O \text{ branch,} \\
 P_Q(J \rightarrow J) &= J(J + 1)/(2J - 1)(2J \\
 &\quad + 3) \rightarrow 1/4 \quad \text{for the } Q \text{ branch,} \\
 P_S(J \rightarrow J + 2) &= 3(J + 1)(J + 2)/2(2J + 1)(2J \\
 &\quad + 3) \rightarrow 3/8 \quad \text{for the } S \text{ branch.}
 \end{aligned} \tag{1}$$

These probabilities are plotted in Fig. 2. Note that the sum of the three branches ( $P_O + P_Q + P_S$ ) for a given  $J$  value is unity as expected. In the classical limit ( $J > 30$ ) the probabilities of the  $O(J)$ ,  $Q(J)$ , and  $S(J)$  branches are, respectively,  $3/8$ ,  $1/4$ , and  $3/8$ , regardless of  $J$  values. Because the relative population of the initial rotational state depends on spin and statistics, the strength of the branches of the

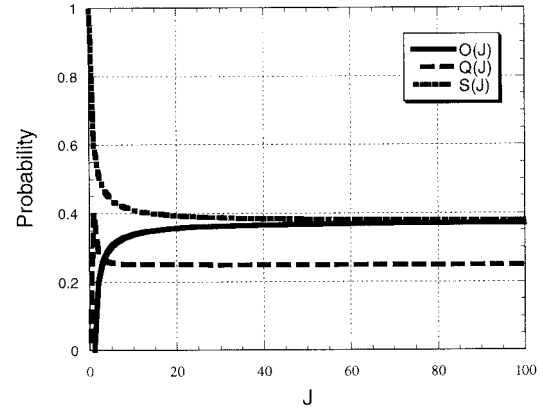


Fig. 2. Placzek and Teller factors, showing the probability of  $O$ -,  $Q$ -, and  $S$ -branch transitions of rotational Raman scattering as a function of the rotational quantum number  $J$ .

depolarized scattering including rotational Raman lines is temperature dependent. The population of the initial state with a given value of nuclear spin  $I$  and rotational quantum number  $J$  is given by

$$\begin{aligned}
 P(J, v) &= (2I + 1)(2J + 1) \\
 &\quad \times \exp[BeJ(J + 1)/(0.6952T)]/Z(T), \tag{2}
 \end{aligned}$$

where

$$\begin{aligned}
 Z(T) &= \sum_{I, J} (2I + 1)(2J + 1) \\
 &\quad \times \exp[-BeJ(J + 1)/(0.6952T)]
 \end{aligned}$$

is the partition function with rotational energy  $E_{\text{rot}} = BeJ(J + 1)$ , with  $Be = 1.998 \text{ cm}^{-1}$  ( $1.438 \text{ cm}^{-1}$ ) for  $N_2$  ( $O_2$ ). The association of  $J$  values for a particular molecular nuclear spin  $I$  is determined by the Pauli exclusion principle and the fact that the ground electronic wave function for  $N_2$  ( $^1\Sigma_g^+$ ) and  $O_2$  ( $^3\Sigma_g^-$ ) are, respectively, even and odd with respect to the interchange of nuclei. The fact that nuclear spins are 1 and 0 for N and O atoms, respectively, gives rise to molecular nuclear spins of  $I = 0, 1$ , and 2 for nitrogen and  $I = 0$  for oxygen molecules. Inasmuch as these diatomic molecules consist of two identical nuclei with integral nuclear spin (1 for N and 0 for O) and with inversion symmetry, their total wave function and vibrational wave function must be even with respect to the interchange of nuclei. For  $N_2$  with an even ground-state electronic wave function, the product of nuclear spin and rotational wave functions must then be even with respect to the interchange of nuclei. Therefore, for nitrogen, the even  $J$  goes with  $I = 0, 2$  (deg = 6) and the odd  $J$  goes with  $I = 1$  (deg = 3); the spectral lines with even  $J$  are twice as intense. For  $O_2$  with an odd ground-state electronic wave function the product of nuclear spin and rotational wave functions must then be odd. Since  $I = 0$  (deg = 1) is the only possibility for oxygen, only rotations with odd  $J$  are allowed. Although the relative strengths of the rotational Raman scattering among

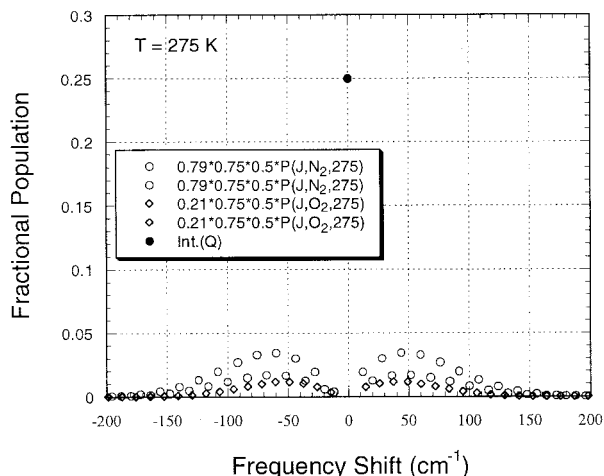


Fig. 3. Pure rotational Raman-scattering spectrum of air including the unshifted component. Note that, owing to the Pauli exclusion principle, the intensity for even  $J$  values is a factor of 2 higher than that for odd  $J$  values in  $N_2$  and only odd  $J$  values are allowed for  $O_2$ . See text for explanation.

$O(J)$ ,  $Q(J)$ , and  $S(J)$  branches should be weighted by the product of  $P(J, \nu)$  in Eq. (2) and the Placzek and Teller factors in Eq. (1), the existence of the rotational degeneracy factor  $(2J + 1)$  in Eq. (2) diminishes the effect of the  $J$  dependence in the Placzek and Teller factor (Fig. 2), lending credence to the classical limit values of  $O(J) = 3/8$ ,  $Q(J) = 1/4$ , and  $S(J) = 3/8$ . With this in mind the probability for the  $Q$  branch in the depolarized scattering spectrum of air is 0.25. Inasmuch as the atmosphere consists of 79% nitrogen and 21% oxygen, the normalized (to unity) relative intensities for the three branches of the depolarized (pure rotational) scattering spectrum can be as plotted in Fig. 3.

A real diatomic molecule vibrates symmetrically with respect to its center of mass. Its associated vibrational-rotational motions scatter light, giving rise to Stokes and anti-Stokes rotational-vibrational sidebands, each consisting of  $O$ ,  $Q$ , and  $S$  branches as shown in Fig. 1. Similar to pure rotational Raman scattering, there are polarized and depolarized scatterings with numerical values of isotropic and anisotropic polarizabilities,  $\alpha_\nu \neq \alpha$  and  $\gamma_\nu \neq \gamma$ . The relative strengths between the  $Q$  branch and the  $O$  and  $S$  branches of the depolarized vibrational Raman scattering are, however, the same as those in the pure rotational Raman scattering given by Eq. (1); in the classical limit they are  $1/4$ ,  $3/8$ , and  $3/8$ , respectively. The lines in the Stokes and anti-Stokes rotational sidebands for the Stokes vibrational sideband are temperature dependent, Eq. (2); they are shown in Fig. 1 for nitrogen molecules at 275 K. At this temperature the intensity of the anti-Stokes vibrational sidebands is too weak to be seen.

To this point we have assumed that the center of mass of a molecule is fixed in space, and only the relative strength of each scattering line resulting from rotational and vibrational motions has been discussed. In practice, each scattering line by itself is a

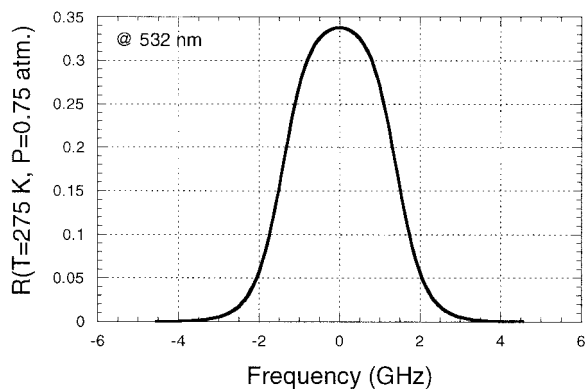


Fig. 4. Doppler-broadened spectrum of the Cabannes line.

frequency spectrum, which to a good approximation can be represented by a broadened (temperature- and pressure-broadened) spectral line shape. Such a line-shape function for the Cabannes scattering, termed incorrectly the Rayleigh-Brillouin spectrum in the bulk of the literature, shall be called here the Cabannes spectrum in honor of Cabannes's discovery of the central peak in the Rayleigh-scattering spectrum. The temperature and the pressure dependence of the Cabannes spectrum can be calculated by the kinetic theory, such as in Tinti *et al.*<sup>14</sup>; a normalized Cabannes spectrum at 532 nm for the atmosphere at 275 K and 0.75 atm is shown in Fig. 4. In the presence of wind the center of this spectrum is Doppler shifted by an amount that depends on wind velocity and scattering direction. In backscattering the Doppler shift is twice the negative of the line-of-sight wind velocity divided by the scattering wavelength, i.e.,  $\Delta\nu = -2V_R/\lambda$ .

### 3. Backscattering Cross Sections of Major Species in the Atmosphere

Along with polarized scattering the differential cross section of the unshifted component and the sum of shifted sidebands of the depolarized scattering can be related in a straightforward manner in terms of polarizability by consideration of radiation from an induced electric dipole moment, as in Appendix A.

For diatomic molecules, such as oxygen and nitrogen, there are only two independent polarizability tensor elements, isotropic (or trace) polarizability  $\alpha$  and anisotropic polarizability  $\gamma$ . For an incident beam with frequency  $\nu$ , linearly polarized, the backward differential cross sections for both parallel and perpendicular components,  $d\sigma_1^R/d\Omega$  and  $d\sigma_2^R/d\Omega$ , are in Appendix A. This gives rise to a total Rayleigh-backscattering differential cross section when both polarization components are received and summed:

$$\begin{aligned} \sigma_\pi^R &= d\sigma_1^R(\pi, \pi/2)/d\Omega + d\sigma_2^R(\pi, \pi/2)/d\Omega \\ &= (\nu\pi^2/\nu_s\lambda_s^4)(\alpha^2 + 7\gamma^2/45) = \sigma_\pi^P + \sigma_\pi^{DP}, \end{aligned} \quad (3)$$

where the two terms in the last expression are, respectively, due to polarized and depolarized backscat-

Table 1. Rayleigh Cross Sections and Derived Anisotropy and Depolarization Ratios at 532 nm

Molecule (Refs.)	Cabannes (m <sup>2</sup> /sr) (×10 <sup>-32</sup> )	Rotational Raman (m <sup>2</sup> /sr) (×10 <sup>-33</sup> )	Rayleigh (m <sup>2</sup> /sr) (×10 <sup>-32</sup> )	Rayleigh Ext. (m <sup>2</sup> ) (×10 <sup>-31</sup> )	King Factor	Anis R <sub>A</sub>	Depolarization Ratio
N <sub>2</sub> (15, 17)	6.02	1.08	6.13	5.31	1.034	0.154	0.0101
O <sub>2</sub> (15, 17)	4.92	2.65	5.19	4.80	1.104	0.470	0.0301
Air (15, 17)	5.96	1.52	6.11	5.37	1.049	0.221	0.0145
Air (19)	5.9	1.5	6.0	5.1	1.049	0.221	0.0145

tering. Note that there are two components in the depolarized scattering: the unshifted (Q branch) and the frequency shifted (O and S branches) with 25% and 75% strengths, respectively, in the classical limit. In the spirit of this paper the unshifted depolarized scattering and the dominant polarized scattering together give rise to the Cabannes scattering, and the shifted (depolarized) scattering is the well-known pure rotational Raman scattering. Their differential backscattering cross sections are

$$\begin{aligned} \sigma_{\pi}^C &= \sigma_{\pi}^P + 0.25 \sigma_{\pi}^{DP} = (\nu\pi^2/\nu_s\lambda_s^4)(\alpha^2 + 7\gamma^2/180) \\ &= \sigma_{\pi}^P(1 + 7R_A/180), \\ \sigma_{\pi}^{RR} &= 0.75 \sigma_{\pi}^{DP} = (\nu\pi^2/\nu_s\lambda_s^4)(21\gamma^2/180) \\ &= \sigma_{\pi}^P(21R_A/180), \end{aligned} \quad (4)$$

respectively, where relative anisotropy and polarized and depolarized differential cross sections are  $R_A = (\gamma/\alpha)^2$ ,  $\sigma_{\pi}^P = (\nu\pi^2/\nu_s\lambda_s^4)\alpha^2$ , and  $\sigma_{\pi}^{DP} = (7/45)\sigma_{\pi}^P R_A$ , respectively.

In lidar measurements it is often of interest to compare the backscatter Rayleigh differential cross section  $\sigma_{\pi}^R$  with that of the averaged (over all directions) differential cross section  $\sigma_T^R$ , which is derived in Appendix A as

$$\begin{aligned} \sigma_{\pi}^R &= \sigma_{\pi}^C + \sigma_{\pi}^{RR} = \sigma_{\pi}^P + \sigma_{\pi}^{DP} = \sigma_{\pi}^P(1 + 7R_A/45), \\ \sigma_T^R &= (\nu\pi^2/\nu_s\lambda_s^4)(2/3)(\alpha^2 + 10\gamma^2/45) \\ &= (2/3)\sigma_{\pi}^P(1 + 10R_A/45). \end{aligned} \quad (5)$$

Thus the total Rayleigh extinction cross section, integrated over all directions, expressed in terms of relative anisotropy  $R_A = (\gamma/a)^2$  is

$$\begin{aligned} \sigma^R &= 4\pi\sigma_T^R = (\nu\pi^2/\nu_s\lambda_s^4)(8\pi/3)\alpha^2 F_K \\ &= (8\pi/3)\sigma_{\pi}^P F_K; F_K = 1 + (2/9)R_A, \end{aligned} \quad (6)$$

where  $F_K$  is the King correction factor.<sup>15</sup> Equation (6) shows clearly that a diatomic molecule with anisotropy scatters more by a factor  $F_K$  owing to incoherent scattering over that owing to polarized (coherent) scattering. It is well known that the isotropic polarizability can be related to refractive index  $n$  and molecular density  $N$  of the atmosphere by noting that  $(n - 1) = 0.5\alpha N$  for dilute gas and that the coherent part of the scattering cross section  $\sigma_{cs}^R$  can be determined from knowledge of  $n$  and  $N$  by

$$\sigma_{cs}^R = (\nu\pi^2/\nu_s\lambda_s^4)(8\pi/3)\alpha^2 = 32\pi^3(n - 1)^2/(3N^2\lambda^4), \quad (7)$$

where the incident wavelength  $\lambda$  and the scattered wavelength  $\lambda_s$  are basically the same for Rayleigh scattering. At STP,  $N = 2.69 \times 10^{25} \text{ m}^{-3}$ , Loschmidt's number. When Eq. (6) is used, the relative anisotropy, the King correction factor, and depolarization ratio  $\delta$  are related as shown in Appendix A:

$$R_A = 4.5(F_K - 1), \quad \delta = 3R_A/(45 + 4R_A). \quad (8)$$

In principle, the polarizability tensor elements  $\alpha$  and  $\gamma$  can be calculated from quantum theory<sup>16</sup> and scattering cross sections can then be estimated. Based on Placzek polarization theory,<sup>12</sup> Inaba<sup>7</sup> has listed the estimates of differential cross sections of Cabannes, pure rotational Raman, and Rayleigh scattering for nitrogen and oxygen molecules at 337.1 nm. The theoretical values listed differ by ~50% from the measured ones. For this reason we use the experimental values for  $\sigma_{\pi}^R$  from Shardanand and Rao,<sup>17</sup> scaled to 532 nm, as compiled by Miles and Nosenchuck,<sup>18</sup> as shown in Table 1, where the values for  $R_A$  are taken from Bridge and Buckingham.<sup>16</sup> By use of Eqs. (6) and (8), the Rayleigh extinction cross section can be computed for air (21% O<sub>2</sub> and 79% N<sub>2</sub>).

Bates<sup>19</sup> published the Rayleigh-scattering cross section and effective King correction factor for air including contributions from minor species between 0.2 and 1 μm from available experimental and theo-

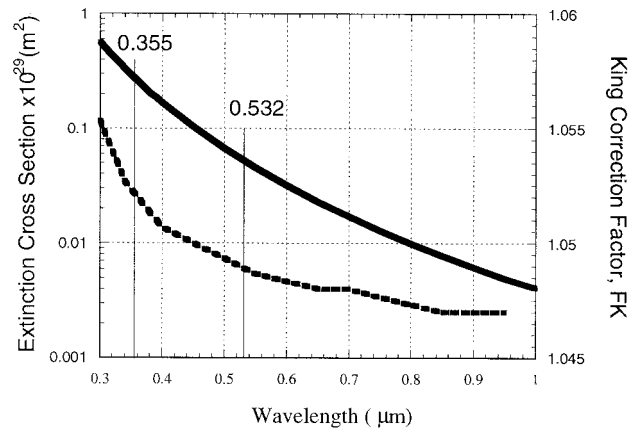


Fig. 5. Total Rayleigh-scattering cross section (in 10<sup>-29</sup> m<sup>2</sup>, solid curve) and the associated King correction factor (dotted curve) as a function of wavelength. They are from Bates<sup>19</sup> and plotted here. The wavelengths of particular interest to lidar operation are marked.

Table 2. Differential Raman Backscattering<sup>a</sup> Cross Sections<sup>b</sup> for N<sub>2</sub>, O<sub>2</sub>, and Air

Molecule (Excitation Wavelength) (nm)	Pure Vibrational dσ <sup>Q</sup> /dΩ (m <sup>2</sup> /sr)	Rotational–Vibrational dσ <sup>O+S</sup> /dΩ (m <sup>2</sup> /sr)	Total Vibrational–Raman dσ <sup>sum</sup> /dΩ (m <sup>2</sup> /sr)
N <sub>2</sub> (377.1)	2.90 × 10 <sup>-34</sup>	5.50 × 10 <sup>-35</sup>	3.45 × 10 <sup>-34</sup>
O <sub>2</sub> (377.1)	3.30 × 10 <sup>-34</sup>	1.30 × 10 <sup>-34</sup>	4.60 × 10 <sup>-34</sup>
Air (377.1)	3.00 × 10 <sup>-34</sup>	7.10 × 10 <sup>-35</sup>	3.71 × 10 <sup>-34</sup>
N <sub>2</sub> (532.0)	4.05 × 10 <sup>-35</sup>	7.67 × 10 <sup>-36</sup>	4.81 × 10 <sup>-35</sup>
O <sub>2</sub> (532.0)	4.83 × 10 <sup>-35</sup>	1.90 × 10 <sup>-35</sup>	6.73 × 10 <sup>-35</sup>
Air (532.0)	4.21 × 10 <sup>-35</sup>	1.01 × 10 <sup>-35</sup>	5.22 × 10 <sup>-35</sup>

<sup>a</sup> $v = 0$  to  $v = 1$ ; 2331 and 1556 cm<sup>-1</sup> for N<sub>2</sub> and O<sub>2</sub>, respectively.

<sup>b</sup>Adapted from Inaba.<sup>7</sup>

retical results. By use of Table 1 I plotted them here as Fig. 5. Reading from Fig. 5 at 532 nm, the second-harmonic wavelength of a YAG laser, we obtain a Rayleigh extinction cross section of  $5.1 \times 10^{-31}$  m<sup>2</sup> and the King correction factor of  $F_K = 1.049$  as given in Table 1. Note that the values given by Bates are in excellent agreement with those compiled by Mile and Nosenchuck,<sup>18</sup> ignoring minor species contributions. Note that the third-harmonic wavelength of a YAG laser, 355 nm, is also a popular wavelength for lidar application. Although the cross section at 355 nm is more than five times larger than that at 532 nm, according to Fig. 5, most Rayleigh lidar employs 532 nm for temperature measurements. This is due to the interference filters being inferior and more absorptive and the aerosol in the atmosphere attenuating more light at 355 nm.

A real diatomic molecule vibrates symmetrically with respect to its center of mass. Scattering by the associated rotational–vibrational motions gives rise to Stokes and anti-Stokes rotational–vibrational sidebands, each consisting of *O*, *Q*, and *S* branches as Fig. 1 suggests. Placzek polarization theory can also be used to estimate the three branches of the rotational–vibrational Raman scattering cross section for the  $v = 0$  to  $v = 1$  transitions excited at 377.1 nm; the result is in Table 5.2 of Inaba<sup>7</sup> in terms of pure vibrational (*Q*-branch) and rotational–vibrational (*O*-branch and *S*-branch) differential cross sections and their sums. These results, which are in reasonably good agreement with the measured values,<sup>7,20</sup> are reproduced and scaled to 532 nm in Table 2. Although a vibrational Raman cross section is weaker than a Rayleigh cross section by 3 orders of magnitude, their frequency dependence is the same and is proportional to  $\nu\nu_s^3$ . The Rayleigh- and Raman-scattering cross sections at 532 nm listed in Tables 1 and 2 are used for discussion and merit evaluation of various nonresonant scattering lidars in Section 4.

#### 4. Cabannes Versus Rayleigh Scattering and Backscatter Ratio

As discussed above where Eq. (3) is expressed in  $(\nu\pi^2/\nu_s\lambda_s^4)$ , the polarized Rayleigh-backscattering differential cross section is  $\alpha^2$ . The corresponding depolarized scattering is  $(7/45)\gamma^2$ . To a good ap-

proximation the relative strengths among the *O*(*J*), *Q*(*J*), and *S*(*J*) branches of depolarized scattering are independent of *J* and are, respectively, 3/8, 1/4, and 3/8. Normalized to the total depolarized backscattering differential cross section of the pure rotational Raman scattering,  $(\nu\pi^2/\nu_s\lambda_s^4)(7/45)\gamma^2$ , the *Q*-branch cross section of the depolarized scattering is 0.25. Therefore, in  $(\nu\pi^2/\nu_s\lambda_s^4)$ , the total unshifted differential cross section is  $\alpha^2 + (0.25)(7/45)\gamma^2$  and the shifted differential cross section is  $(0.75)(7/45)\gamma^2$ . Including the trace scattering, the total unshifted backscattering is 29.47 in the same unit. The unshifted differential cross section amounts to 97.5% of the total strength based on  $(\gamma/\alpha)^2 = 0.22$ ; the shifted pure rotational Raman scattering amounts to 2.5%.

An important quantity in lidar measurement of aerosol and cloud is determination of the backscatter ratio *R* defined as the ratio of the total backscattering coefficient [aerosol  $\beta_a(z)$  plus molecular  $\beta_m(z)$ ] to that due to Rayleigh (molecular) scattering  $\beta_m(z)$  as

$$R = [\beta_a(z) + \beta_m(z)]/\beta_m(z) = 1 + [\beta_a(z)/\beta_m(z)], \quad (9)$$

where  $\beta_m(z) = n(z)\sigma_\pi^R$  with  $\sigma_\pi^R$  and  $n(z)$  as, respectively, the differential Rayleigh-backscattering cross section and molecular density at altitude *z*. In the lidar literature whether the shifted rotational Raman scattering and (vibrational) Raman scattering are included in the definition of molecular scattering is often not specified. By use of the definition of the backscatter ratio in Eq. (9), vibrational Raman scattering, which is negligible anyway, can be excluded. Depending on the bandwidth of a lidar receiver, the shifted pure rotational Raman scattering signal can or might not be included in the measurement of the backscatter ratio. The difference between the use of Cabannes- and Rayleigh-backscattering cross sections in the backscatter ratio calculation can lead to a potential error in the determined backscatter ratio by 2.5%. Ironically, the HSRL, which is capable of measuring the aerosol-mixing ratio directly and accurately detects only Cabannes scattering, thus overestimates the backscatter ratio by the said amount. Because this fact is known, the error can be corrected easily.

**Table 3. Relative Signal Strength and Bandwidth Comparison between Different Scattering Lidar for Atmospheric Parameter Measurements**

Backscatter Lidar	Measured Parameters (Method)	Relative Signal Strength <sup>a</sup>	Receiver Bandwidth <sup>a</sup> Night (Day)	Comments
Mie	Aerosol and cloud	>1	5 nm (100 GHz)	Bandwidth for night (day) detection
Aerosol wind	Wind (HET or FPI)	>1	1 GHz, FSR	Filter bandwidth (resolution), ~0.1 GHz Frequency stability, 1 ms <sup>-1</sup> /4 MHz
Rayleigh	Temperature (Inversion)	1	5 nm (100 GHz)	Must be aerosol free Bandwidth for night (day) detection
HSRL	Temperature (AVF; Ratio)	0.2	10 GHz	Frequency stability, 0.6 K/2 MHz Good aerosol rejection
HSRL	Aerosol and wind (AVF; Ratio)	0.4	10 GHz	Frequency stability, 1 ms <sup>-1</sup> /4 MHz
Rotational Raman	Temperature (IF; Ratio)	0.005	5 nm	Filter bandwidth, ~1 nm, Frequency and filter stability, 10 GHz Filter optical density >6 at laser wavelength Daytime operation difficult
Vibrational Raman	Backscatter Extinction	0.001	3 nm (500 GHz)	No broader than 5 nm at night
Vibrational Raman	Temperature (Inversion)	0.001	5 nm (100 GHz)	Bandwidth for night (day) detection Problematic with extinction gradient
Molecular Wind	Wind and temperature (Double FPI)	0.1	10 GHz, FSR	Problematic with aerosol Filter bandwidth (resolution), ~1 GHz Frequency stability, 1 ms <sup>-1</sup> /4 MHz

<sup>a</sup>See text for the definitions of HET, FPI, AVF, IF, and FSR.

### 5. Bandwidth and Signal-Strength Comparisons among Scattering Lidars

Using the results in Sections 3 and 4, we can compare the merits of various types of scattering lidar in terms of their bandwidths and signal strengths.

From Tables 1 and 2 the differential cross sections for Rayleigh, Cabannes, shifted rotational Raman, and total vibrational Raman scattering, excited at 532 nm, are  $6.0 \times 10^{-32}$ ,  $5.9 \times 10^{-32}$ ,  $1.5 \times 10^{-33}$ , and  $5.2 \times 10^{-35}$  m<sup>2</sup>/sr, respectively. Assuming a comparable loss owing to receiving optics, we can estimate the relative signal from these cross sections for Rayleigh lidar, HSRL, RRL, and vibrational Raman lidar (VRL), respectively. Relative to Rayleigh scattering, the approximate cross sections of Cabannes, shifted rotational Raman scattering, and vibrational Raman scattering are 1, 0.025, and 0.001, respectively. An additional factor of 5 from Cabannes and shifted rotational Raman cross sections are applied in Table 3 to reduce the signal strength in HSRL and RRL, because the signals used to retrieve atmospheric parameters in these cases are the ratio of lidar returns in two receiving channels, and, in addition, narrow-band filters (atomic vapor filters<sup>21</sup> for HSRL and interference filters for RRL) are used in the receiver, further reducing the scattered light. With the presence of aerosol and clouds as in Mie and

aerosol-wind lidars, the relative signal strength could be much greater than unity.

Also listed in Table 3 is the receiver bandwidth (in gigahertz or in nanometers at  $\lambda = 532$  nm) typically used in each lidar. Since the Rayleigh-scattering spectrum is the sum of the Cabannes line and shifted pure rotational Raman lines, its total bandwidth is  $\sim 200$  cm<sup>-1</sup> ( $\sim 5$  nm). In the absence of aerosol (Mie) scattering the receiver bandwidth of a Rayleigh lidar at night is thus  $\sim 5$  nm when an interference filter with  $\sim 5$  or 10 nm FWHM is used. Because the strength of the shifted rotational Raman scattering is  $\sim 2.5\%$  of the strength of the Cabannes line, one could use a 10-GHz receiver bandwidth without losing much signal for daytime detection; in practice a custom-designed and fabricated interference filter (IF) of 0.1-nm (or 100-GHz) bandwidth can be used. By the same token the receiver bandwidth for Mie and VRLs can be typically 5 and 0.1 nm, respectively, for night and day operation. Because in both lidars near-elastic aerosol scattering (in the case of Mie lidar) and the Q branch of vibrational Raman scattering (in the case of VRL), respectively, dominate the lidar return, a narrower receiver bandwidth should be employed in the daytime to reject sky background. Inasmuch as a broader bandwidth is necessary for temperature measurements with rotational Raman

lidar, daytime operation is difficult. On the other hand, temperature measurements with HSRL depend on the Cabannes line, and aerosol- and molecular-wind measurements depend on Mie and Cabannes lines, respectively. Using direct detection with either a Fabry–Perot interferometer (FPI) or an atomic vapor filter (AVF) require an ultranarrow-band ( $\sim 10$ -GHz) receiver system suitable for daytime detection. The price is in the stability of both the transmitter frequency and the receiver filter. In the case of wind measurements the common wisdom is to use  $1.064 \mu\text{m}$  with either coherent heterodyne (HET) or direct detection for aerosol-based and  $355 \text{ nm}$  with direct detection for molecular-based line-of-sight wind measurements to take advantage of strong aerosol scattering at a longer wavelength and strong Cabannes (molecular) scattering at a shorter wavelength. For direct detection, depending on wavelength, FPIs with a different free spectral range (FSR) are used as frequency discriminators. When both aerosol and molecular scatterings are important, it could be advantageous to use  $532 \text{ nm}$  with an atomic vapor filter for frequency discrimination. Although different wavelengths can be used for temperature and wind measurements, it suffices to estimate the required frequency stabilities based on  $532 \text{ nm}$  as in Table 3.

Note that the detectability of the lidar signal and the measurability of an individual atmospheric parameter depend on the signal-to-noise ratio.<sup>22</sup> However, the detection noise is not discussed in detail in this paper, except to point out that with photon counting the dominating noise consists of photon noise from the sky background and noise that is due to the interference of an undesired signal. Photon noise is intrinsic and its adverse effect can be reduced only by integration (or an increase in measurement time). The background noise can be reduced by the use of narrow-band filters to match the bandwidth of the desired signal. Only the relative signal strengths of scattering lidars have been compared, and the bandwidth of receiving filters that differ for daytime and nighttime lidar applications are listed in Table 3. To reduce the interference of undesired signals, a high stability in transmitting laser frequency and receiving filters are required; the system stability thus plays an essential role in narrow-band lidar operations and is often a key to successful data acquisition with HSRL and RRL. For daytime operation the pointing stability of the transmitting beam, with fractional millirad divergence to minimize the detected sky background, is also important. A well-engineered lidar system that could be automated<sup>23</sup> is not only cost-effective in the long run but absolutely necessary if long-term (daytime) observation from either a ground-based or spaceborne lidar is desired.

## 6. Summary

A brief review of various spectral components of molecular scattering in terms of their individual scattering strengths and bandwidths is presented. The confusion in the literature with regard to the correct

name for each scattering process is revisited, decomposing the Rayleigh-scattering spectrum into the central Cabannes line and pure rotational Raman sidebands. A step-by-step simple description of various scattering cross sections and the associated King correction factor, scattering ratios, and depolarization ratio in terms of polarizability tensor elements and relative anisotropy of air molecules have been presented. A clear spectral description and relationships between cross sections of different scattering components allow a systematic comparison of relative scattering strengths and receiver bandwidths (for nighttime and daytime operation) between different nonresonant scattering lidars for atmospheric sensing of the backscatter ratio, temperature, and wind. A systematic comparison in a specific bandwidth requirement, signal strength, merits, and measurement capabilities between Mie, aerosol-wind, Rayleigh, HSRL, molecular-wind, rotational Raman, and vibrational Raman lidars are in Table 3. The inability to distinguish Cabannes scattering from Rayleigh scattering could result in a 2.5% error in backscatter ratio measurements. The strength of the Cabannes line is relatively great compared with Raman sidebands. Using it for atmospheric temperature and wind measurements, however, requires use of an ultra-narrow-band transmitter and receiver system whose stability is difficult to maintain. On the other hand, Raman scattering is relatively weak, and the associated broadband spectrum renders daytime measurement difficult and wind measurement impossible. The concise tabulation provides, it is hoped, not only a systematic characterization of a molecular-scattering spectrum but also a practical and useful guide for those who are interested in or conduct research with various types of scattering lidar.

## Appendix A: Backscattering Cross Sections and Depolarization Ratio

The differential scattering cross section can be derived in a straightforward manner by considering dipole radiation from an induced electric dipole moment  $\mathbf{p}$ . According to electromagnetic theory,<sup>24</sup> the radiated power per unit solid angle is

$$\begin{aligned} dP/d\Omega &= (ck_s^4/32\pi^2\epsilon_0)|(\hat{n} \times \mathbf{p}) \times \hat{n}|^2 \\ &= (\pi^2c/2\epsilon_0\lambda_s^4)|(\hat{n} \times \mathbf{p}) \times \hat{n}|^2, \end{aligned} \quad (\text{A1})$$

where  $\hat{n}$ ,  $\nu_s$ , and  $\lambda_s$  are unit vectors in scattered direction, frequency, and wavelength, respectively. For an induced dipole the polarizability tensor can be defined as  $p_i = \epsilon_0\alpha_{ij}E_j$ , where  $p_i$  and  $E_j$  are Cartesian components of induced dipole moment and inducing electric field, respectively, with  $\epsilon_0$  and  $\alpha_{ij}$  ( $\alpha_{ij}$  in cubic meters) as vacuum permittivity and polarizability matrix elements. The intensity of the incident inducing field is  $I = (c\epsilon_0/2)|E|^2$ .

For diatomic molecules, such as oxygen and nitrogen, there are only two independent polarizability tensor elements,  $\alpha_{\parallel}$  and  $\alpha_{\perp}$ , which can be written in terms of isotropic (or trace) polarizability,  $\alpha = (\alpha_{\parallel} +$

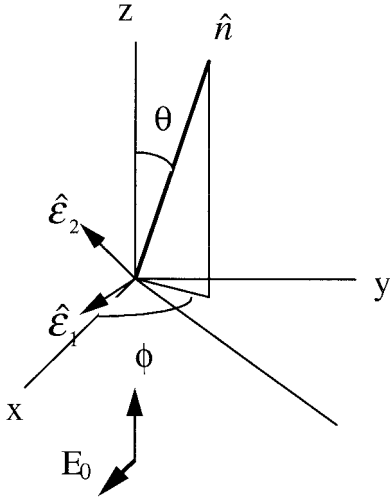


Fig. 6. Scattering geometry. The incident beam is polarized in the  $x$  direction and propagates along the  $z$  axis. The scattered light propagates along  $\hat{n}$  with two perpendicular polarizations along  $\hat{\epsilon}_1$  and  $\hat{\epsilon}_2$ .

$2\alpha_{\perp})/3$ , and anisotropic polarizability,  $\gamma = (\alpha_{\parallel} - \alpha_{\perp})$ . For an incident beam with frequency  $\nu$ , linearly polarized in the  $x$  direction, the induced dipole moment on a diatomic molecule will have projections in all three Cartesian directions; one can calculate their relative strengths in the classical limit by averaging over random orientation of air molecules. As shown in Fig. 6 the resultant differential scattering cross section (defined on the basis of photons) for the scattered light at scattered frequency  $\nu_s$  along the direction  $\hat{n}(r, \theta, \phi)$ , which can be decomposed into two independent polarizations,  $\hat{\epsilon}_1$  (on the  $x$ - $y$  plane and perpendicular to  $\hat{n}$ ) and  $\hat{\epsilon}_2$  (perpendicular to both  $\hat{n}$  and  $\hat{\epsilon}_1$ ), is given for each component as

$$d\sigma^R(\theta, \phi)/d\Omega = (\nu\pi^2/\nu_s\lambda_s^4)[(\gamma^2/15)(\epsilon_y^2 + \epsilon_z^2) + (\alpha^2 + 4\gamma^2/45)\epsilon_x^2], \quad (\text{A2})$$

where the incident and the scattered frequency,  $\nu$  and  $\nu_s$ , in general need not be the same. The quantities  $\epsilon_x$ ,  $\epsilon_y$ , and  $\epsilon_z$  are the direction cosines of the scattered electric vectors,  $\hat{\epsilon}_1 = (\sin \phi, -\cos \phi, 0)$  and  $\hat{\epsilon}_2 = (-\cos \theta \cos \phi, -\cos \theta \sin \phi, \sin \theta)$ . The differential cross sections for the two perpendicularly polarized components are

$$\begin{aligned} d\sigma_1^R(\theta, \phi)/d\Omega &= (\nu\pi^2/\nu_s\lambda_s^4)[(\gamma^2/15)\cos^2\phi \\ &\quad + (\alpha^2 + 4\gamma^2/45)\sin^2\phi], \\ d\sigma_2^R(\theta, \phi)/d\Omega &= (\nu\pi^2/\nu_s\lambda_s^4) \\ &\quad \times [(\gamma^2/15)(\cos^2\theta \sin^2\phi + \sin^2\theta) \\ &\quad + (\alpha^2 + 4\gamma^2/45)\cos^2\theta \cos^2\phi]. \end{aligned} \quad (\text{A3})$$

A special case typically considered for laboratory experiments is the case of  $90^\circ$  scattering with vertically polarized input as discussed by Young.<sup>4</sup> One can obtain the scattering cross sections for this case from

Eq. (A3) by setting  $\theta = \pi/2$  and  $\phi = \pi/2$ , yielding results in agreement with those shown in Table 2 of Ref. 4:

$$d\sigma_1^R(\pi/2, \pi/2)/d\Omega = (\nu\pi^2/\nu_s\lambda_s^4)(\alpha^2 + 4\gamma^2/45)$$

for vertically scattered  ${}^vT_v$ ,

$$d\sigma_2^R(\pi/2, \pi/2)/d\Omega = (\nu\pi^2/\nu_s\lambda_s^4)(\gamma^2/15) \quad (\text{A4})$$

for horizontally scattered  ${}^vT_h$ .

Another special case of considerable importance to lidar application is that of backscattering along  $z$  with the incident  $E$  field along  $x$ . One can obtain the scattering cross sections by choosing  $\theta = \pi$  and  $\phi = \pi/2$ , yielding for parallel and perpendicularly polarized scattering

$$\begin{aligned} \sigma_{1,\pi}^R &= d\sigma_1^R(\pi, \pi/2)/d\Omega = (\nu\pi^2/\nu_s\lambda_s^4)(\alpha^2 \\ &\quad + 4\gamma^2/45), \\ \sigma_{2,\pi}^R &= d\sigma_2^R(\pi, \pi/2)/d\Omega = (\nu\pi^2/\nu_s\lambda_s^4)(\gamma^2/15), \end{aligned} \quad (\text{A5})$$

respectively. Ironically, the differential cross sections for these two important cases are the same. The total Rayleigh-backscattering differential cross section when both components are received and summed is

$$\begin{aligned} \sigma_{\pi}^R &= d\sigma_1^R(\pi, \pi/2)/d\Omega + d\sigma_2^R(\pi, \pi/2)/d\Omega \\ &= (\nu\pi^2/\nu_s\lambda_s^4)(\alpha^2 + 7\gamma^2/45) \\ &= (\nu\pi^2/\nu_s\lambda_s^4)\{[\alpha^2 + 0.25(7\gamma^2/45)] \\ &\quad + 0.75(7\gamma^2/45)\} = \sigma_{\pi}^C + \sigma_{\pi}^{RR}, \end{aligned} \quad (\text{A6})$$

where, in the spirit of this paper, the first term is referred to as Cabannes scattering and the second term as rotational Raman scattering (the shifted branches). To separate polarized scattering from depolarized scattering, we define their differential cross sections as

$$\begin{aligned} \sigma_{\pi}^P &\equiv d\sigma^P(\pi, \pi/2)/d\Omega = (\nu\pi^2/\nu_s\lambda_s^4)\alpha^2, \\ \sigma_{\pi}^{DP} &\equiv d\sigma^{DP}(\pi, \pi/2)/d\Omega = (\nu\pi^2/\nu_s\lambda_s^4)(7\gamma^2/45), \end{aligned} \quad (\text{A7})$$

respectively.

In lidar measurements it is often of interest to compare the backscatter differential cross sections,  $\sigma_{1,\pi}^R$ ,  $\sigma_{2,\pi}^R$ , and  $\sigma_{\pi}^R$  with the averaged differential cross section (over all directions)  $\sigma_T^R$ , which can be calculated by noting that

$$\langle \cos^2 \phi \rangle = (1/4\pi) \int \cos^2 \phi d\Omega = \langle \sin^2 \phi \rangle = 0.5,$$

$$\langle \cos^2 \theta \rangle = 1/3, \quad \langle \sin^2 \theta \rangle = 2/3,$$

$$\langle \cos^2 \theta \sin^2 \phi \rangle = \langle \cos^2 \theta \cos^2 \phi \rangle = 1/6,$$

as

$$\begin{aligned}\sigma_T^R &= (1/4\pi) \int [\mathrm{d}\sigma_1^R(\theta, \phi)/\mathrm{d}\Omega + \mathrm{d}\sigma_2^R(\theta, \phi)/\mathrm{d}\Omega] \mathrm{d}\Omega \\ &= (\nu\pi^2/\nu_s\lambda_s^4)(2/3)(\alpha^2 + 10\gamma^2/45).\end{aligned}\quad (\text{A8})$$

Thus the total Rayleigh (extinction)-scattering cross section, integrated over a  $4\pi$  solid angle, expressed in terms of relative anisotropy  $R_A = (\gamma/a)^2$  and the King correction factor  $F_K$  is

$$\begin{aligned}\sigma^R &= 4\pi\sigma_T^R = (\nu\pi^2/\nu_s\lambda_s^4)(8\pi/3)\alpha^2(1 + 10R_A/45) \\ &= (\nu\pi^2/\nu_s\lambda_s^4)(8\pi/3)\alpha^2F_K,\end{aligned}\quad (\text{A8})$$

where  $F_K = 1 + (2/9)R_A$ . The ratios of the backscatter differential cross sections to the averaged differential cross section can be given as respective  $q$  factors:

$$\begin{aligned}q_1^R(\pi) &\equiv \sigma_{1,\pi}^R/\sigma_T^R \\ &= (1.5)(\alpha^2 + 4\gamma^2/45)/(\alpha^2 + 10\gamma^2/45), \\ q_2^R(\pi) &\equiv \sigma_{2,\pi}^R/\sigma_T^R = (1.5)(\gamma^2/15)/(\alpha^2 + 10\gamma^2/45), \\ q^R(\pi) &\equiv q_1^R(\pi) + q_2^R(\pi) \\ &= (1.5)[1 - (\gamma^2/15)/(\alpha^2 + 10\gamma^2/45)],\end{aligned}\quad (\text{A9})$$

and the depolarization ratio as

$$\begin{aligned}\delta &\equiv \sigma_{2,\pi}^R/\sigma_{1,\pi}^R = (\gamma^2/15)/(\alpha^2 + 4\gamma^2/45) \\ &= 3R_A/(45 + 4R_A).\end{aligned}\quad (\text{A10})$$

Most of this research was done at the Radio Atmospheric Science Center (RASC), Kyoto University, during my sabbatical in 1999. The suggestion and facilitation of T. Tsuda and T. Nakamura for a lecture series on lidar measurement and lidar science during my stay, which provided the seed and indeed much of the material for this paper, are gratefully acknowledged. Beneficial e-mail exchanges and discussions with colleagues elsewhere, P. Keckhut, K. Fricke, E. Eloranta, A. Behrendt, C. Nakasawa, H. Moosmüller, G. Herring, J. Hair, and D. Krueger and the able assistance of M. Abe during the course of lecture preparation, are also gratefully acknowledged.

## References

1. J. Cabannes, "Un nouveau phénomène optique: le battement qui se produit lorsque des molécules anisotropes en rotation et vibration diffusent de la lumière visible ou ultraviolette," *C. R. Acad. Sci.* **186**, 1201–1202 (1928).
2. J. Cabannes and Y. Rocard, "La Théorie électromagnétique de Maxwell-Lorentz et la diffusion moléculaire de la lumière," *J. Phys. Rad.* **10**, (6) 52–71 (1929).
3. A. Hauchecorne and M.-L. Chanin, "Density and temperature profiles obtained by lidar between 35 and 70 km," *Geophys. Res. Lett.* **78**, 565–568 (1980).
4. A. T. Young, "Rayleigh scattering," *Phys. Today* 42–48 (January 1982).
5. I. L. Feblinskii, *Molecular Scattering of Light* (Plenum, New York, 1968).
6. H. Rosen, P. Robrish, and O. Chamberlain, "Remote detection of pollutants using resonance Raman scattering," *Appl. Opt.* **14**, 2703–2706 (1975).
7. H. Inaba, "Detection of atoms and molecules by Raman scattering and resonance fluorescence," in *Laser Monitoring of the Atmosphere*, E. D. Hinkley, ed. (Springer-Verlag, Berlin, 1976), pp. 153–236.
8. R. M. Schotland, "Errors in the lidar measurement of atmospheric gases by differential absorption," *J. Appl. Meteorol.* **13**, 71–77 (1974).
9. C. Y. She, H. Latifi, J. R. Yu, R. J. Alvarez II, R. E. Bills, and C. S. Gardner, "Two-frequency lidar technique for mesospheric Na temperature measurements," *Geophys. Res. Lett.* **17**, 929–932 (1990).
10. H. Edner, J. Johansson, S. Svanberg, and E. Wallinder, "Fluorescence lidar multicolor imaging of vegetation," *Appl. Opt.* **33**, 2471–2479 (1994).
11. R. Loudon, *The Quantum Theory of Light*, 2nd ed. (Clarendon, Oxford, 1983), Chap. 8.
12. G. Placzek, *Handbuch der Radiologie, Vol. 6, Part 2*, E. Marx, ed. (Akademischer Verlag, Leipzig, 1934).
13. R. Gaudres and S. Sportouch, "The Placzek-Teller coefficients  $b_{J,K}^{J,K}$  for negative  $\Delta J$ ," *J. Mol. Spectrosc.* **39**, 527–530 (1971).
14. G. Tenti, C. D. Boley, and R. C. Desai, "On the kinetic model description of Rayleigh-Brillouin scattering from molecular gases," *Can. J. Phys.* **52**, 285–290 (1974).
15. L. V. King, "On the complex anisotropic molecule in relation to the dispersion and scattering of light," *Proc. R. Soc. London A* **104**, 333–357 (1923).
16. N. J. Bridge and A. D. Buckingham, "The polarization of laser light scattered by gases," *Proc. R. Soc. London Sect. A* **295**, 334–349 (1966).
17. Shardanand and A. D. Prasad Rao, "Absolute Rayleigh-scattering cross sections of gases and freons of stratospheric interest in the visible and ultraviolet regions," NASA TN D-8442 (March 1977).
18. R. B. Miles and D. M. Nosenchuck, "Three-dimensional quantitative flow diagnostics," in *Lecture Notes in Engineering: Advances in Fluid Dynamics Measurement*, (Springer-Verlag, Berlin, 1989), pp. 33–107.
19. D. R. Bates, "Rayleigh scattering by air," *Planet. Space Sci.* **32**, 785–790 (1984).
20. H. W. Schrötter and H. W. Köckner, "Raman scattering cross sections in gases and liquids," in *Raman Spectroscopy of Gases and Liquids*, Topics in Current Applied Physics, A. Weber, ed. (Springer-Verlag, Berlin, 1979), p. 123.
21. J. W. Hair, L. M. Caldwell, D. A. Krueger, and C.-Y. She, "High spectral resolution lidar with iodine vapor filters: measurement of atmospheric state and aerosol profiles," *Appl. Opt.* (to be published).
22. R. W. Boyd, *Radiometry and the Detection of Optical Radiation* (Wiley, New York, 1983), Chap. 8.
23. U. von Zahn, G. von Cossart, J. Fiedler, K. H. Fricke, G. Nelke, G. Baumgarten, D. Rees, A. Hauchecorne, and K. Adolfsen, "The ALOMAR Rayleigh/Mie/Raman lidar: objectives, configuration, and performance," *Ann. Geophys.* **18**, 815–833 (2000).
24. J. D. Jackson, *Classical Electrodynamics*, 2nd ed. (Wiley, New York, 1975), p. 369.